CONFRONTING COLD DARK MATTER PREDICTIONS WITH OBSERVED GALAXY ROTATIONS

Danail Obreschkow[1], Xiangcheng Ma[2], Martin Meyer[1,3], Chris Power[1,3], Martin Zwaan[4],
Lister Staveley-Smith[1,3], and Michael J. Drinkwater[5]
[1] International Centre for Radio Astronomy Research (ICRAR), M468, University of Western Australia, 35 Stirling Hwy, Crawley, WA 6009, Australia
[2] The University of Sciences and Technology of China, Centre for Astrophysics, Hefei, Anhui 230026, China
[3] ARC Centre of Excellence for All-sky Astrophysics (CAASTRO)
[4] European Southern Observatory, Karl-Schwarzschild-Str. 2, D-85748 Garching b. München, Germany
[5] School of Mathematics and Physics, The University of Queensland, Brisbane, QLD 4072, Australia

ABSTRACT

The rich statistics of galaxy rotations as captured by the velocity function (VF) provide invaluable constraints on galactic baryon physics and the nature of dark matter (DM). However, the comparison of observed galaxy rotations against cosmological models is prone to subtle caveats that can easily lead to misinterpretations. Our analysis reveals full statistical consistency between ∼5000 galaxy rotations, observed in line-of-sight projection, and predictions based on the standard cosmological model (ΛCDM) at the mass-resolution of the Millennium simulation (H I line-based circular velocities above ∼50 km s^{-1}). Explicitly, the H I linewidths in the H I Parkes All Sky Survey (HIPASS) are found to be consistent with those in S^3-SAX, a post-processed semi-analytic model for the Millennium simulation. Previously found anomalies in the VF can be plausibly attributed to (1) the mass-limit of the Millennium simulation, (2) confused sources in HIPASS, (3) inaccurate inclination measurements for optically faint sources, and (4) the non-detectability of gas-poor early-type galaxies. These issues can be bypassed by comparing observations and models using linewidth source counts rather than VFs. We investigate if and how well such source counts can constrain the temperature of DM.

Key words: dark matter – galaxies: kinematics and dynamics – galaxies: statistics – ISM: atoms – ISM: kinematics and dynamics – radio lines: galaxies

Online-only material: color figures

1. INTRODUCTION

Mass and angular momentum are crucial galaxy properties, since their global conservation laws constrain the history and future of galaxy evolution (Bullock et al. 2001a, 2001b). Moreover, measurements of mass and angular momentum uncover hidden dark matter (DM) and potentially constrain its nature (Zavala et al. 2009; Obreschkow et al. 2013). In recent decades, the mass statistics have been studied in detail via the mass function (MF; Li & White 2009), the luminosity function (LF; Loveday et al. 2012), and the auto-correlation function (Blake et al. 2011). By contrast, angular momentum remains a side-topic, normally addressed indirectly via the Tully–Fisher relation (TFR; McGaugh 2012) or used as a means of recovering the mass distribution in individual galaxies (de Blok et al. 2008). Spatial statistics of angular momentum and the related circular velocity function (VF; Gonzalez et al. 2000; Desai et al. 2004; Zwaan et al. 2010; Papastergis et al. 2011) remain relatively unexplored. This is despite the fact that the VF offers tremendous potential with regard to comparing LFs obtained in different wave-bands (Gonzalez et al.), measuring various mechanisms of feedback in the evolution of galaxies (Sawala et al. 2012), and constraining the temperature of DM (Zavala et al. 2009).

In fact, measuring a galaxy's rotational velocity is challenging, since it requires both a measurement of the galaxy inclination, typically drawn from a spatially resolved optical image, as well as a measurement of the line-of-sight rotational velocity, typically obtained from the Doppler-broadening of the 21 cm emission line of neutral hydrogen (H I). Today, only two H I surveys offer reasonably large samples to construct VFs, the H I Parkes All Sky Survey (HIPASS; Barnes et al.

2001) and the ongoing Arecibo Legacy Fast ALFA (ALFALFA; Giovanelli et al. 2005a, 2005b). They are the largest surveys by the cosmic volume and by the number of galaxies, respectively. The VFs derived from HIPASS (Zwaan et al. 2010) and the 40%-release of ALFALFA (Papastergis et al. 2011) were both compared against theoretical models, including predictions by the S^3-SAX-model (Obreschkow et al. 2009a), the only current model of frequency-resolved H I-emission lines in a cosmological simulation. These comparisons uncovered statistically significant differences, some of which could be attributed to gas-poor massive early-type galaxies (Zwaan et al. 2010), but the physical implications remained unclear. Differences in the faint-end of the VF (Figure 9 in Papastergis et al. 2011), near the resolution limit of the S^3-SAX-model, seemed to hint at a possible breakdown of the current cosmological model. In a new attempt to understand and exploit these differences, we successively found them to be subtle artifacts of the comparison itself, hence motivating a more detailed analysis.

This paper presents a revised comparison between the H I line profiles in HIPASS and S^3-SAX. We deliberately focus on HIPASS, while reserving a similar analysis of the ongoing ALFALFA survey for the future, because HIPASS already has optical inclinations available, exhibits a detailed completeness function, and contains less cosmic variance than 40%-ALFALFA in terms of the redshift-distribution of the galaxies (see Figure 4(a) by Martin et al. 2010 versus Figure 2 (bottom) by Zwaan et al. 2005). The HIPASS data is compared against the S^3-SAX-model in various ways. A key result, worth highlighting early, is the full consistency between the 50-percentile H I linewidth W_{50} in HIPASS and S^3-SAX, as illustrated by the counts in Figure 1. In this work, we compare both apparent
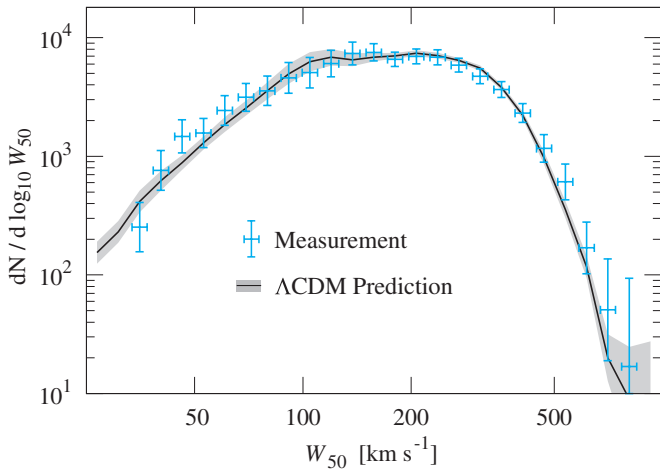
Figure 1. Counts of H I linewidths in the largest equivalent subsamples of the HIPASS survey and the ΛCDM-based S³-SAX-model. This plot shows that measured and simulated linewidths agree on the completeness domain of $M_{H I} \gtrsim 10^8 M_\odot$ and $V_c \gtrsim 50 \, km \, s^{-1}$. Error bars represent 67%-measurement uncertainties associated with actual measurement noise, cosmic variance, and completeness uncertainties. Similarly, the gray shading depicts 67%-confidence intervals for the model, associated with cosmic variance. This figure is a simplified version of Figure 5(b).

(A color version of this figure is available in the online journal.)

H I linewidths and inclination-corrected circular velocities using source counts, as well as space density functions. The different aspects uncovered by these functions are discussed in detail, as well as their reliability as statistical estimators. Based on the results, we finally conjecture that linewidth counts might be a useful tool for measuring the temperature of DM, and discuss how well HIPASS can, in principle, constrain this temperature.

The manuscript is organized as follows. Section 2 first explains the observed data set (HIPASS with optical imaging) and its simulated counterpart (S³-SAX). Five statistically independent simulations are generated specifically to assess the effects of cosmic variance. The observed and simulated data sets are then truncated to congruent subsamples suitable for their comparison. This comparison is presented in detail in Section 3. In Section 4, the consistency between HIPASS and S³-SAX is interpreted and discussed with respect to the TFR and alternative models of DM. Section 5 summarizes the results in a list of key messages.

2. DATA DESCRIPTION

2.1. Observed Data: HIPASS

HIPASS is a blind search for H I emission at declinations decl. $< +25°$ in the velocity range $-1280 \, km \, s^{-1} < cz < 12,700 \, km \, s^{-1}$, where c is the speed of light and z is the redshift. This survey resulted in 5317 identified galaxies, gathered in two catalogs: the HIPASS galaxy catalogue (HICAT; Meyer et al. 2004; Zwaan et al. 2004), containing 4315 sources with decl. $< +2°$, and its northern extension (NHICAT; Wong et al. 2006), containing 1002 sources with $+2° <$ decl. $< +25°$. The H I lines of these 5317 sources have been parameterized in various ways. In this work, we will use the luminosity distance D_L, given in Mpc, the velocity-integrated line flux S_{int}, given in Jy km s^{-1}, the corresponding H I mass $M_{H I} = 2.36 \times 10^5 S_{int} D_L^2 (1+z)^{-1}$, given in $M_\odot$, the peak-flux density S_p, given in mJy, and the linewidth W_{50} ("W_{50}^{max}" in HICAT), given in km s^{-1} and measured at 50% of the peak flux density. HIPASS uses a channel width of 13.2 km s^{-1}, but parameterization was carried out after two

stages of smoothing (Tukey and Hanning), resulting in a full-width-half-max resolution of 26.4 km s^{-1} for W_{50}.

Doyle et al. (2005) presented optical counterparts for HICAT, identified in the b_J-band plates of the SuperCOSMOS Sky Survey (Hambly et al. 2001). To each of these galaxies, they fitted an ellipse to measure the semi-major axis a, the semi-minor axis b, and the position angle. There are 3618 sources in HOPCAT with identified values a and b. From those values, the galaxy inclinations i can be estimated using the spheroid assumption,

$$\cos^2 i = \frac{q^2 - q_0^2}{1 - q_0^2}, \quad (1)$$

where $q \equiv b/a$ and q_0 denotes the intrinsic axis ratio, here taken to be $q_0 = 0.2$ to remain consistent with Zwaan et al. (2010). As in the latter work, we here *define* the circular velocity V_c of a galaxy as

$$V_c \equiv \frac{W_{50}}{2 \sin i}, \quad (2)$$

although the actual asymptotic rotational velocity may slightly differ from V_c.

2.2. Simulated Data: S³-SAX

This section summarizes S³-SAX (Obreschkow et al. 2009a), the first cosmological model of resolved H I-emission lines of galaxies.

S³-SAX builds on model-galaxies generated by a semi-analytic model (SAM; De Lucia & Blaizot 2007). The latter relies on the Millennium simulation (Springel et al. 2005) that tackles the evolution of cold dark matter (CDM) in a comoving box measuring $(500 \, h^{-1} \, Mpc)^3$, where h is defined via the local Hubble constant $H_0 \equiv 100 \, h \, km \, s^{-1} \, Mpc^{-1}$. This simulation uses the standard cosmological model (ΛCDM) with parameters $h = 0.73$, $\Omega_m = 0.25$, $\Omega_b = 0.045$, $\Omega_\Lambda = 0.75$, and $\sigma_8 = 0.9$. From this simulation, CDM halos and their merging histories are extracted. The SAM then assigns galaxies to the centers of these halos using a cooling model and evolves global galaxy properties, such as stellar mass, gas mass, and morphology according to physical rules allowing for feedback from black holes and supernovae. The free parameters in this SAM were tuned to the locally observed color—magnitude distribution, but there is no explicit fit to galaxy sizes, rotations, and gas properties. The number of model-galaxies at a time of 13.7×10^9 yr, i.e., today, is to about 3×10^7. Although the cosmological parameters of the Millennium simulation are slightly inconsistent with the newest estimates (Komatsu et al. 2011), the present-day galaxy properties remain nearly unaffected according to calculations by Guo et al. (2013).

Given the evolving model-galaxies of the SAM, Obreschkow et al. (2009a) assigned refined cold gas properties to each galaxy. Their method, sketched out in Figure 2, can be summarized as follows. The scale radius of galactic disks is calculated directly from the spin of the DM halo. To do so, a variable ratio $\xi \in [0.5–1]$ between the specific angular momentum of baryons and DM was adopted. This ratio is a function of the Hubble-type and the stellar mass, adjusted such that the resulting disk scale radii optimally reproduce those of the real galaxies in The H I Nearby Galaxy Survey (THINGS; Walter et al. 2008). Given the disk scale radius and the total cold gas mass from the SAM, the radial H I surface density $\Sigma_{H I}(r)$ is calculated using a pressure-based model for the ratio between molecular (H_2) and atomic (H I) hydrogen (Obreschkow & Rawlings 2009), derived from the THINGS sample (Leroy et al. 2008). In parallel, circular
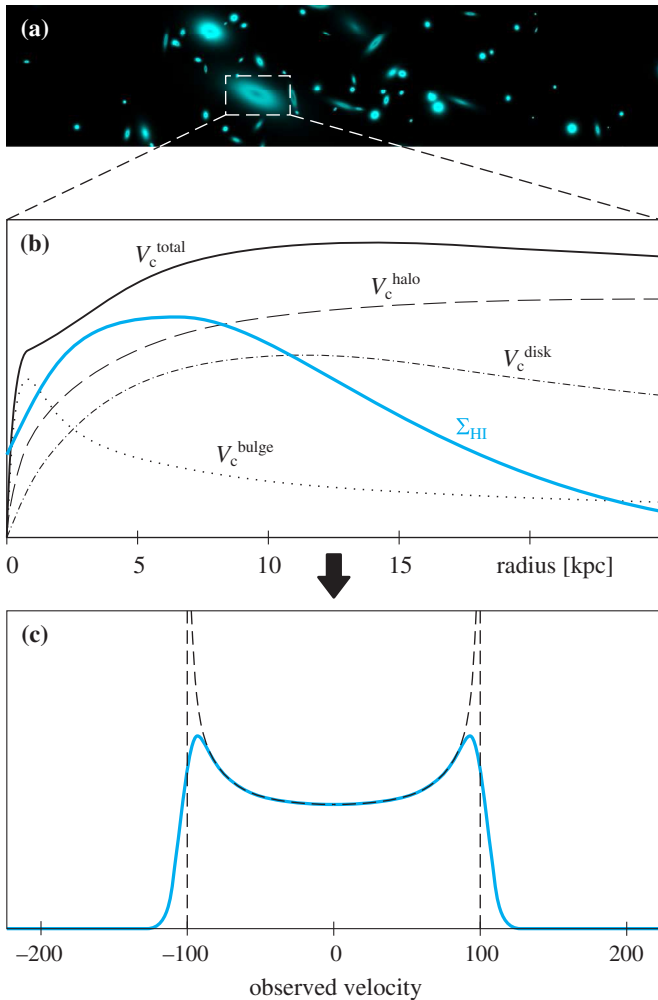
Figure 2. Illustration of our method to model H I emission lines. For each model galaxy, we compute an axially symmetric H I density profile $\Sigma_{H_I}(r)$ and a circular velocity profile $V_c^{total}(r)$ based on mass distribution in the halo, disk, and bulge. Convolving $\Sigma_{H_I}(r)$ with $V_c^{total}(r)$ yields an ideal edge-on emission line (panel (c), dashed line), which is smoothed with a Gaussian Kernel of $\sigma = 8\,km\,s^{-1}$ to account for the velocity dispersion typical for the local universe (panel (c), solid line).

velocity profiles $V_c^{total}(r) = (V_c^{halo^2}(r) + V_c^{disk^2}(r) + V_c^{bulge^2}(r))^{1/2}$ are calculated from the circular velocities implied by the gravitational potentials of the DM halo, the galactic disk, and the central bulge, respectively. Convolving $V_c^{total}(r)$ with $\Sigma_{H_I}(r)$ then results in a model for the frequency-resolved H I emission line (dashed line in Figure 2(c)), which, when convolved with a Gaussian Kernel for dispersion, turns into a smooth profile (solid line).

Departing from the cubic box of the Millennium simulation populated with model-galaxies with resolved H I emission lines, Obreschkow et al. (2009b) produced a sky-model with apparent extra-galactic H I emission as seen by a fixed observer. To do so, the Cartesian coordinates (x, y, z) of the model-galaxies were mapped onto apparent positions, i.e., right-ascension (R.A.), declination (decl.), and redshift z, using the method of Blaizot et al. (2005). This method explicitly accounts for the fact that galaxies more distant from the observer are seen at an earlier stage in their cosmic evolution. Along with this mapping, the intrinsic H I luminosities are transformed into observable fluxes. Moreover, the H I emission line of each galaxy is corrected for the inclination of the galaxy, respecting, however, the isotropy
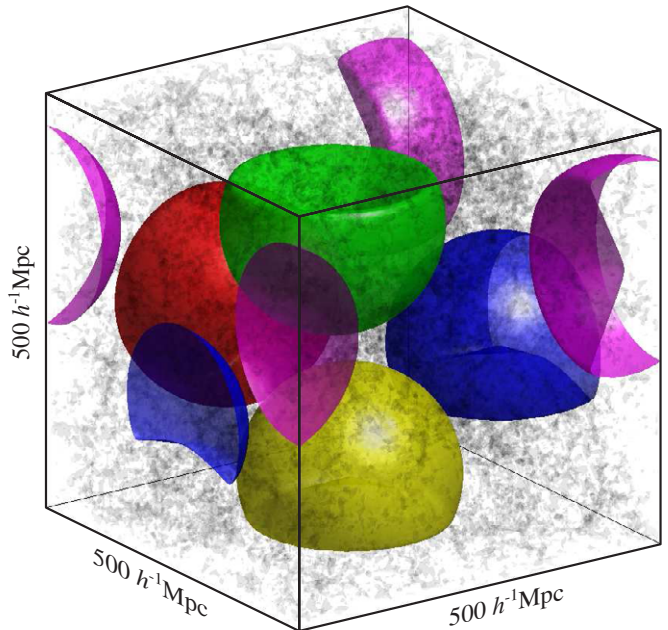
Figure 3. The five colors represent our five virtual HIPASS volumes fitted inside the cubic box of the Millennium simulation. The box obeys periodic boundary conditions, such that the truncated volumes (blue and purple) are in fact simply connected. The five HIPASS volumes do not overlap and can hence be used to estimate the magnitude of cosmic variance.

of turbulent/thermal dispersion. The linewidth W_{50} at the 50%-level of the peak flux density is then measured from the apparent H I line of the inclined model galaxy. To allow a clean comparison with observations, we then calculate the circular velocity V_c of a model galaxy via Equation (2). This is an important step, since V_c can differ from the asymptotic value of $V_c^{total}(r \to \infty)$ by up to 30% for some galaxies with relatively compact H I distributions.

For the purpose of this paper, we realized five different virtual skies by placing the cosmic volume probed by HIPASS five times inside the simulation box of the Millennium simulation as shown in Figure 3. There is no overlap between these five sub-volumes, making them (almost) statistically independent. These five virtual sky volumes will be used to quantify the effects of cosmic variance, that is, the random effects of the locally inhomogeneous large scale structure.

When comparing the S^3-SAX-model against HIPASS, it is crucial to note that the gridded beam of the HIPASS data measures 15ʹ.5 at full-width-half-max. Using the S^3-SAXsky-model, we find that this limited spatial resolution implies a non-negligible probability for two or more H I disks to be confused, i.e., to fall inside the same beam and simultaneously overlap in frequency. Hence, this confusion must be accounted for when comparing observations against simulations. We do so by merging simulated galaxies, whose centroids are separated by less than 15ʹ.5 and whose H I lines overlap in frequency. The common H I mass is then taken as the sum of the individual components and W_{50} is measured from the combined line as shown in Figure 4. We further define the circular velocity V_c of the merged object as the H I mass-weighted average of the circular velocities of the components. This procedure reduces the number of simulated sources by about 2%.

2.3. Sample Selection

Let us now construct subsamples of sources in HIPASS and S^3-SAX using identical selection criteria. Two types of samples

sky view　　　　　　　spectrum
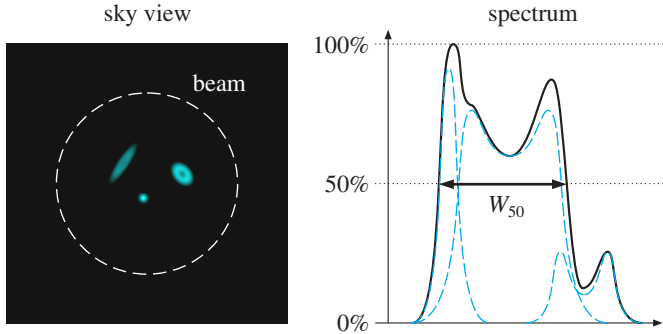
Figure 4. Simulated galaxies with centers separated by less than the FWHM of the HIPASS beam of 15.'5 (left panel) and with H I emission lines overlapping in frequency at the 20-percentile level (dashed lines, right panel) are regarded as confused. For comparison with HIPASS, such confused sources are considered as a single sources with an emission line (solid line) obtained by co-adding the individual constituents.

(A color version of this figure is available in the online journal.)

Table 1
The Upper List Shows the Criteria Applied to all Data Presented in This Paper

Selection Criterion	Trims HIPASS	Trims S^3-SAX
Reference sample:		
decl. $\leqslant +25°$	No	Yes
$cz <= 12{,}700\,\mathrm{km\,s^{-1}}$	No	Yes
$M_{\mathrm{H\,I}} \geqslant 10^8\,h_{70}^{-1}\,M_\odot$	Yes	Yes
$W_{50} \geqslant 25\,\mathrm{km\,s^{-1}}$	No	Yes
$C(S_{\mathrm{p}}, S_{\mathrm{int}}) \geqslant 0.5$	Yes	Yes
$C(S_{\mathrm{p}}, S_{\mathrm{int}}) \geqslant R$	No	Yes
Additional criteria for V_c-sample:		
decl. $\leqslant +2°$	Yes	Yes
$0.86 \geqslant R$	No	Yes
$i \geqslant 45°$	Yes	Yes

Notes. The lower list shows the additional selection criteria applied when comparing circular velocities V_c, which require optical inclination measurements. Here, $R \in [0, 1]$ denotes a random number drawn separately for every galaxy and equation.

will be considered depending on whether optical counterparts are required for HIPASS sources. These counterparts are needed when considering circular velocities V_c, since those require estimates of the galaxy inclinations. However, masses $M_{\mathrm{H\,I}}$ and linewidths W_{50} do not require optical data. We shall call the larger galaxy sample, in which optical counterparts are irrelevant, the "reference sample." A subsample of this reference sample, in which all galaxies have optical inclinations and thus estimates of V_c, is then called the "V_c-sample." The precise selection criteria of these two samples are listed in Table 1 and explained in the following.

2.3.1. Reference Sample

Volume truncation. Since the volume of S^3-SAX exceeds that of HIPASS, the former must be truncated to the field-of-view and redshift range of HIPASS, i.e., decl. $\leqslant +25°$ and $cz \leqslant 12{,}700\,\mathrm{km\,s^{-1}}$. These criteria truncate S^3-SAX to sub-volumes matching the colored regions in Figure 3.

Mass limit. The limiting H I mass, above which S^3-SAX can be considered complete, is about $10^8\,h_{70}^{-1}\,M_\odot$ (Obreschkow et al. 2009a), where $h_{70} \equiv h/0.7$, i.e., $h_{70} = 1$ if $H_0 = 70\,h\,\mathrm{km\,s^{-1}\,Mpc^{-1}}$, as consistent with current observations (Jarosik et al. 2011). The simulated H I MF drops rapidly below this limiting mass due to the limited mass resolution of the Millennium simulation. We must therefore limit the comparison between simulated and observed sources to the mass range $M_{\mathrm{H\,I}} \geqslant 10^8\,h_{70}^{-1}\,M_\odot$. This criterion removes 71 nearby galaxies from HIPASS, that is, about 1.3% of the 5317 identified sources.

Limiting linewidth. HIPASS does not resolve sources with linewidths smaller than $25\,\mathrm{km\,s^{-1}}$ (see Section 3.1 in Meyer et al. 2004). For correctness, we therefore apply the selection criterion $W_{50} \geqslant 25\,\mathrm{km\,s^{-1}}$ to S^3-SAX, although this only reduces the number of simulated sources by about 0.1%.

Completeness limit. In HIPASS, real sources are detected with a probability approximated by

$$C(S_{\mathrm{p}}, S_{\mathrm{int}}) = E[p_1(S_{\mathrm{p}} - p_2)]E[p_3(S_{\mathrm{int}} - p_4)], \qquad (3)$$

where $E(x) \equiv \max\{0, \mathrm{erf}(x)\}$. The parameters are $\mathbf{p} = (0.036, 19, 0.36, 1.1)$ for decl. $\leqslant +2°$ (Zwaan et al. 2004) and $\mathbf{p} = (0.02, 5, 0.14, 1)$ for decl. $> +2°$ (Wong et al. 2006). The same completeness function must be applied to S^3-SAX. This is done by drawing a random number R uniformly from

the interval $[0, 1]$ for every simulated galaxy, and retaining the galaxy only if $C(S_{\mathrm{p}}, S_{\mathrm{int}}) \geqslant R$. In addition, we must account for the fact that the completeness function itself is very uncertain for $C(S_{\mathrm{p}}, S_{\mathrm{int}}) < 0.5$ (e.g., Figure 6 in Zwaan et al. 2004). As in Zwaan et al. (2010), we therefore only retain galaxies with $C(S_{\mathrm{p}}, S_{\mathrm{int}}) \geqslant 0.5$. These completeness cuts reduce the total number of simulated sources in the HIPASS volume to about 8%, while reducing the number of observed sources by 514, i.e., by an additional 9.8% after the 1.3% mass cut. This concludes the construction of the reference samples.

2.3.2. V_c-sample

To compare observed and simulated values of V_c, the reference sample must be further reduced to a HOPCAT equivalent sample, i.e., a subsample with optically measured inclinations.

Volume truncation. We must exclude the galaxies with decl. $> +2°$, for which optical inclinations are not readily available in HIPASS. In doing so, the number of observed and modeled objects shrinks by roughly 20%.

HOPCAT completeness. Out of all galaxies in the reference sample with decl. $\leqslant +2°$, only 86% yield optical inclinations. Most of the remaining objects lie too close to the galactic plane, where the stellar foreground deteriorates extragalactic optical imaging. To account for this incompleteness, we reduce the number of simulated galaxies to 86% by only retaining the objects satisfying $0.86 \leqslant R$, where $R \in [0, 1]$ is a random number.

Inclination selection. Galaxies with inclinations close to face-on exhibit poor inclination measurements, which, given their small values of i, result in highly uncertain values of V_c when using Equation (2). As in Zwaan et al. (2010), we therefore only retain galaxies with $i \geqslant 45°$, hence reducing the sample sizes by an additional 29%.

3. COMPARISON BETWEEN HIPASS AND S^3-SAX

Given the identically selected samples of observed and simulated galaxies, we shall now compare the statistics of the H I line profiles. This comparison will be carried out both at the level of direct source counts (Section 3.2) and at the level of space density functions (Section 3.3).

Table 2
Number of Sources in Each Sample

	Reference Sample	V_c-sample
Observation	4732	2352
Simulation 1	4699	1839
Simulation 2	5268	2194
Simulation 3	5034	2103
Simulation 4	4212	1642
Simulation 5	5416	2285

Note. The selection criteria are listed in Table 1 and the simulated volumes are shown in Figure 3.

3.1. Sample Size

Let us first consider the raw size of the observed and simulated samples given in Table 2.

The mean number of sources in the five simulated reference samples is about 4926, with a standard deviation of 482. This standard deviation is significantly higher than the Poisson shot noise of $\sim\sqrt{4926} \approx 70$, demonstrating the non-negligible effect of large scale structure in HIPASS. The number of observed sources in the reference sample is clearly consistent with the simulation. We therefore expect the normalization of corresponding source count statistics and space density functions to be consistent between observation and simulation.

By contrast, the mean number of sources in the simulated V_c-samples (about 2013) undershoots the number of observed sources by about 339 or 14%. This difference is slightly larger than the characteristic value of cosmic variance of 267, estimated from the standard deviation of the object numbers in the five simulated V_c-samples. As argued in Section 3.2, this moderately significant difference between the sizes of the observed and simulated V_c-samples is at least partially explainable by a small fraction of inaccurate inclination measurements in HOPCAT. Those tend to assign high inclinations ($i \geqslant 45°$) to

objects, which in actual fact have low inclinations ($i < 45°$) and should hence be removed from the observed V_c-sample.

3.2. Source Counts

A refined statistical analysis consists of counting the number of galaxies, binned by specific galaxy properties. The properties of particular interest are the H I linewidth W_{50} and the circular velocity V_c defined by Equation (2). For completeness, we also analyze the statistics of the H I mass M_{HI}. The source counts of M_{HI} and W_{50} are derived from the reference samples. In turn, the source counts of V_c, which require inclination measurements, must be performed using the smaller V_c-samples.

Figures 5(a)–(c) show the observed (bars) and simulated (lines) counts of M_{HI}, W_{50}, and V_c, respectively. The gray solid lines correspond to the five individual simulations, while the black lines represent the geometric means of these functions. Variations between the five models are due to cosmic variance. The observed source counts exhibit several error bars, representing the uncertainties described in Table 3. Some of these uncertainties are statistical, while others are systematic and thus correlated across different bins.

The observed and simulated M_{HI} counts in Figure 5(a) are moderately consistent. Four of the five models and the mean model show a slight bump around $M_{HI} \approx 4 \times 10^8 M_\odot$. This seems to be a feature of the particular SAM chosen here, since it is also present in the b_J-band LF of the same SAM (see Figure 8 right of Croton et al. 2006) but is absent in other SAMs building on the Millennium simulation (e.g., Baugh et al. 2005).

Figure 5(b) is the central plot of this paper and extends on Figure 1. It demonstrates that the simulated linewidths W_{50} are fully consistent with the observed ones. We emphasize that this consistency requires that the simulated and observed samples are constructed according to identical selection criteria (see Table 1). Experimenting with different completeness functions C further revealed the importance of using the smooth completeness function $C(S_p, S_{int})$ provided for HICAT and NHICAT. A

Table 3
Explanation of the Different Error Bars Shown in Figure 5

Error Name	Type	Explanation
Cosmology uncertainty (h)	Systematic	Variations of the Hubble parameter h on the interval [0.65, 0.75]. This interval contains the fiducial value of $h = 0.704^{+0.013}_{-0.014}$ (7-year WMAP+BAO, Jarosik et al. 2011), as well as the recently found $h = 0.743 \pm 0.021$ (Spitzer and Hubble space telescope, Freedman et al. 2012). Note that it is important to plot h-related uncertainties, since observed and simulated data scale differently with h; e.g., simulated masses are in units of $h^{-1}M_\odot$, while observed masses are in units of $h^{-2}M_\odot$.
Completeness uncertainty	Systematic	Approximate 67%-confidence intervals associated with systematic uncertainties of the completeness function C (see Equation (3)) in the range $C > 0.5$. We calculate these uncertainties as $\Delta C = 0.4(1 - C)/C$, which approximately matches the error bars in Figures 2 and 6 of Zwaan et al. (2004). Note that variations in the completeness function would alter the simulated data rather than the observed data. In Figure 5, these error bars have only been plotted on the observed data for graphical convenience.
Cosmic variance	Statistical	67%-confidence intervals associated with cosmic variance, as determined from the standard deviation between the five simulated samples.
Shot noise	Statistical	Approximate 67%-confidence intervals associated with Poisson shot noise, calculated as the square root of the number of sources in the bin.
Direct measurement noise	Statistical	Approximate 67%-confidence intervals associated with telescope noise and limited frequency resolution (Section 2.1).
Distance errors	Statistical	67%-confidence intervals associated with errors in the spectroscopic distance measurement, assuming average line-of-sight peculiar velocities of 300 km s^{-1}. This uncertainty is largest from nearby sources and therefore largest for low-mass galaxies in HIPASS.

Notes. The error "type" refers to whole sample. For example, distance errors due to peculiar velocities are systematic for an individual source, but statistical at the level of a sample of sources with random peculiar motions. In combining multiple errors into a single error bar, statistical errors are added in quadrature, while systematic errors are added linearly.
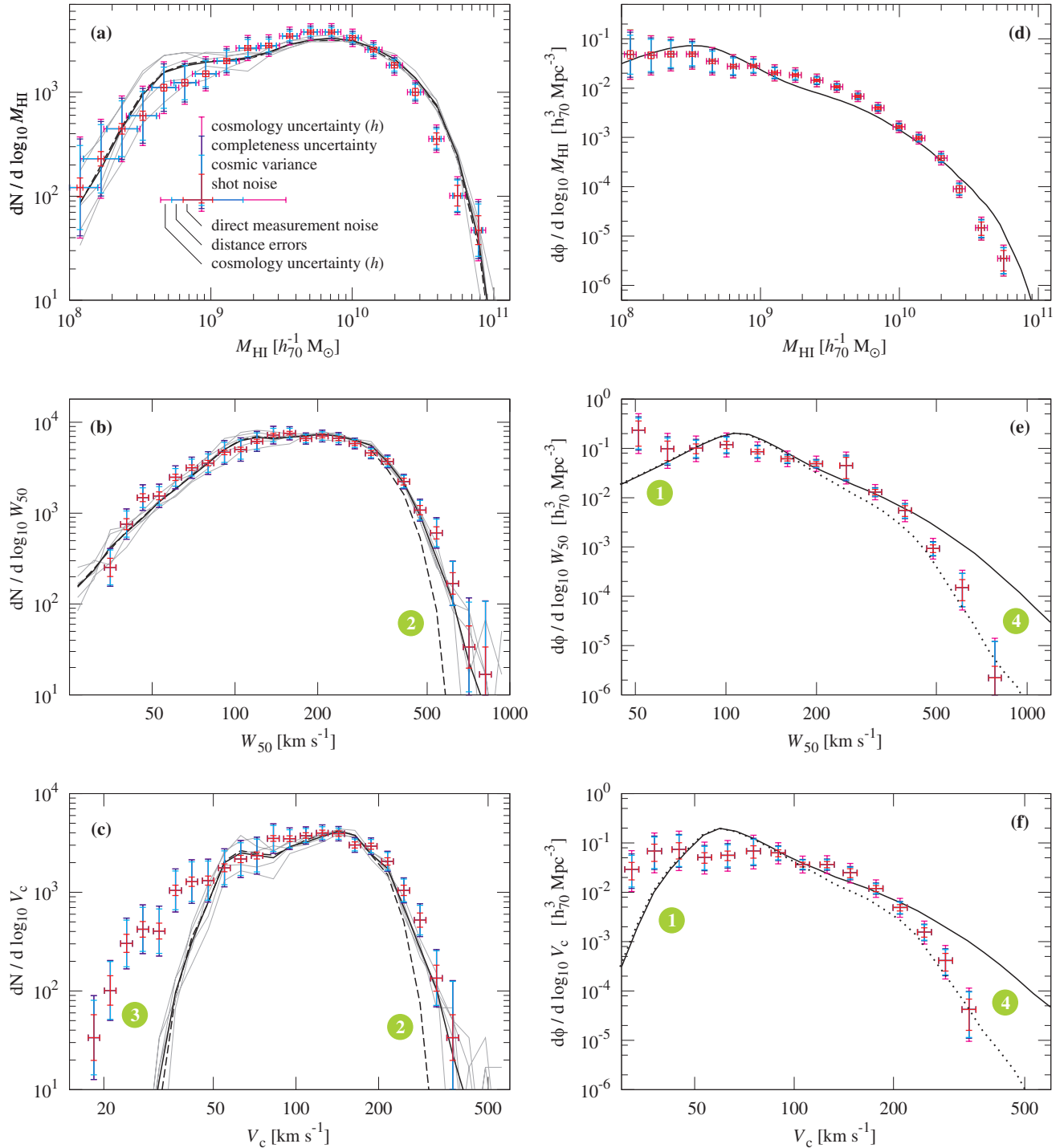
Figure 5. Statistical comparison between HIPASS and S³-SAX. Error bars represent various measurement uncertainties described in Table 3. Thin gray solid lines represent the five statistically independent simulations, while the thick solid lines represent their geometric averages. Dashed lines delineate the same averages if source-confusion is not accounted for. Dotted lines represent only late-type galaxies, excluding S0 and E-types. Green numbers denote artifacts discussed in Section 3; they match the numbers in the abstract. (a) counts of masses M_{HI} in the reference samples; (b) counts of linewidths W_{50} in the reference samples; (c) counts of circular velocities $V_c \equiv W_{50}/(2\sin i)$ in the V_c-samples; (d) H I MF as derived from HICAT by Zwaan et al. (2005) and predicted using all model-galaxies in the Millennium box; (e) space density function of W_{50} for galaxies of all Hubble-types as derived from HICAT by Zwaan et al. (2010) and predicted using all model-galaxies; (f) H I VF for galaxies of all Hubble-types with inclinations $i \geqslant 45°$ as derived from HICAT and HOPCAT by Zwaan et al. (2010) and predicted using all model-galaxies. Since the observed data points use all Hubble-types, the data in panels (e) and (f) must be compared against the solid function. The dotted function (only late-types) nonetheless provides a better fit, because the predicted class of gas-poor early-types was simply not detectable by HIPASS (details in Section 3.3).

(A color version of this figure is available in the online journal.)

hard sensitivity limit, i.e., $C(S_p, S_{int})$ as a step-function, is not sufficient in that it induces variations larger than the error bars. Moreover, accounting for the confusion of sources turns out to be vital. If, instead, all individual galaxies in the simulated sky

were considered distinguishable, then the mean source counts are given by the dashed line in Figure 5(b). The difference is most pronounced at the largest linewidths of $W_{50} \gtrsim 500\,\text{km s}^{-1}$ (artifact "2"). Thus, the largest values of W_{50} in the observed
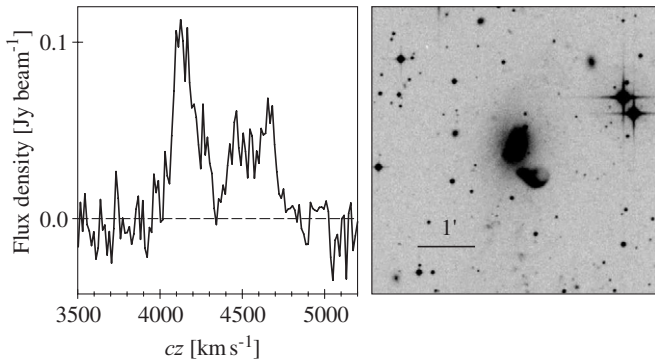
Figure 6. Example of a typical confused source in HICAT. This object (HIPASSJ1347-30) was assigned a single width of $W_{50} = 653.6\,\mathrm{km\,s^{-1}}$ (without confusion flag), the highest value of any source with $S_{\mathrm{int}} > 50\,\mathrm{Jy\,km\,s^{-1}}$. The SuperCOSMOS optical b_J-band image suggests that the H I emission line is a combination of two merging systems.

data are mostly due to confused sources, i.e., galaxies within the same telescope beam and with H I line profiles overlapping in frequency space. In constructing the original HICAT data set (Meyer et al. 2004), an effort was made to flag and separate sources exhibiting confused H I line profiles. About 9% of the sources with $W_{50} \geqslant 500\,\mathrm{km\,s^{-1}}$ in the reference sample have been flagged as confused (as opposed to 7% in the whole reference sample). By contrast, our modeling revealed that most sources with $W_{50} \geqslant 500\,\mathrm{km\,s^{-1}}$ are confused. This means that

it may be impossible to identify most instances of confusion by relying exclusively on the information in the HIPASS data. An example of a confused source is shown in Figure 6.

The counts of circular velocities V_c are shown in Figure 5(c). The models are consistent with the observations for $V_c > 50\,\mathrm{km\,s^{-1}}$, but drastically differ for smaller velocities (artifact "3"). The only major difference between Figures 5(b) and (c) is the inclination-correction (see Equation (2)); therefore, the excess of observed sources with $V_c < 50\,\mathrm{km\,s^{-1}}$ suggests an issue with their inclinations. A systematic visual inspection of the b_J-band images of the SuperCOSMOS Sky Survey used in HOPCAT uncovered that a vast majority (>90%) of the galaxies with $V_c < 50\,\mathrm{km\,s^{-1}}$ (about 11% of the 2352 objects in the V_c-sample or 6% of all 4315 galaxies in HICAT/HOPCAT) are problematic. They are either too faint or too irregular for an optical estimation of the inclination, or they simply exhibit erroneous shape parameterizations. Figure 7 displays three representative examples of the latter case. The ellipses in Figure 7 represent the original parameterization in terms of minor axis, major axis, and position angle. The axis ratios of these ellipses imply inclinations $i > 45°$ (via Equation (1)). To the naked eye, however, these three galaxies are nearly face-on spiral disks ($i < 45°$), especially in the multi-color image of the source HIPASSJ1200-00, which is about two magnitudes deeper than SuperCOSMOS. Using the "correct" inclination for this source rather than that suggested by HOPCAT increases V_c roughly by a factor two. Since the correct inclination is then below 45°, this source would be rejected from the V_c-sample and
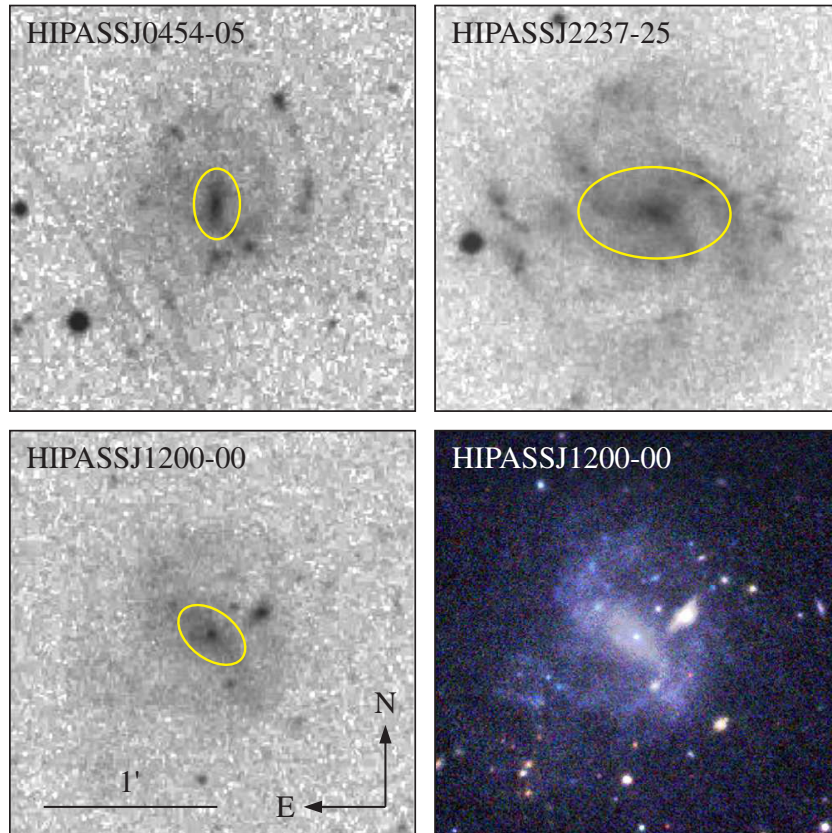
Figure 7. Three examples of the few galaxies in HOPCAT (about 6% of all HICAT/HOPCAT objects) with uncertain/inaccurate shape parameterizations. The three gray-scale images are the b_J-band maps from the SuperCOSMOS Sky Survey (Hambly et al. 2001) used in HOPCAT, while the false-color image (i-band in red, r-band in green, g-band in blue) shows a corresponding deep image obtained by the Galaxy And Mass Assembly (GAMA) survey (Driver et al. 2011). Yellow ellipses represent the fits quoted in HOPCAT; they all overestimate the inclinations of the galaxies. (Note that position angles in HOPCAT are given anti-clockwise from west rather than north.)

(A color version of this figure is available in the online journal.)

thus disappear from Figure 5(c). In conclusion, there is a small fraction of incorrect shape identifications in HOPCAT, which happens to dominate the low-end of the V_c counts. Incidentally, this also explains the asymmetric scatter skewed toward low rotational velocities in the HOPCAT-based TFR (upper panels in Figure 3 in Meyer et al. 2008).
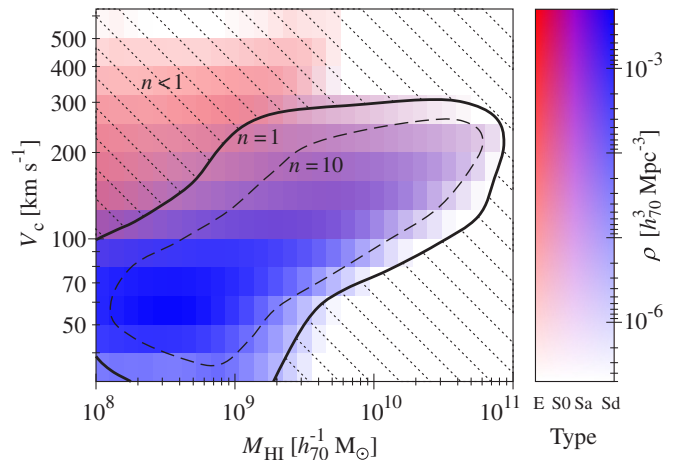
3.3. Space Densities

The source counts presented in the previous section depend on the selection criteria of the survey listed in Table 1. Survey-independent, and thus more fundamental statistical measures, are the space density functions $\phi \equiv dN/dV$. These functions represent the absolute number of sources, detected or not, per unit of cosmic volume and per unit of galaxy properties, such as M_{HI} (H I MF) or V_c (VF). Evaluating these functions from empirical data requires inverting the completeness function, as well as removing the effects of cosmic variance. This is achieved by the two-dimensional stepwise maximum likelihood (2DSWML) method developed by Zwaan et al. (2003) and applied by Zwaan et al. (2005, 2010) to recover the observed space density functions of M_{HI}, W_{50}, and V_c, shown in Figures 5(d)–(f). Note that the data shown here include all Hubble-types. Figures 5(d)–(f) also display the simulated counterparts (solid lines), obtained simply by binning all galaxies contained in the redshift $z = 0$ box of the Millennium simulation. This box is large enough for cosmic variance to be neglected. However, the observed space density functions still obey the same cosmic variance as the respective source counts. Therefore, the cosmic variance uncertainty is plotted with the observed data, although we derive its value from the variations between the five simulated source counts.

Figure 5(d) reveals that the simulated and observed H I MFs are only marginally consistent in the sense that the simulation falls within the error bars for about 50% of the data points rather than 67%. The fact that the agreement was slightly better in the source count statistics of Figure 5(a) might indicate a minor artifact in the reconstruction of the observed H I MF. For example, as suggested by Zwaan et al. (2004), the "true" completeness function C exhibits a slight dependence on the shape of the H I line profile (single-peaked, double-peaked, flat-top) in addition to the main dependence on S_p and S_{int}. This small higher-order effect could be captured by extending the 2DSWML method to 3D using $C(S_p, S_{int}, shape)$.

Figures 5(e) and (f) suggest clear inconsistencies between the models and observations. In the small velocity range, these inconsistencies (artifact "1") directly relate to the mass resolution limit of the Millennium simulation. This limit implies a significant incompleteness of simulated objects with $W_{50} \lesssim 80 \, km \, s^{-1}$ and $V_c \lesssim 50 \, km \, s^{-1}$ (and $M_{HI} < 10^8 M_\odot$ to the left of Figure 5(d)). In turn, this mass-limit is probably linked to the spurious bumps around $W_{50} \approx 120 \, km \, s^{-1}$ and $V_c \approx 70 \, km \, s^{-1}$.

A more subtle feature in Figures 5(e) and (f) are the significant deviations at $W_{50} \gtrsim 500 \, km \, s^{-1}$ and $V_c \gtrsim 200 \, km \, s^{-1}$ (artifact "4"). Those deviations are absent in the corresponding source counts of Figures 5(b) and (c). A systematic investigation of the simulated galaxies in this high-velocity regime reveals them to be dominated by early-type galaxies of numerical Hubble-type $T \leqslant 0$ (E, S0) hosting low-mass, but fast-rotating H I disks. Excluding those objects from the simulation modifies the predicted functions in Figures 5(e) and (f) to the dot-dashed lines, which are in much better agreement with the observed data, as already noted by Zwaan et al. (2010). In other words, the model predicts that the high-end of the

Figure 8. Predicted space density $\rho(M_{HI}, V_c)$ per pixel of size $\Delta \log_{10} M_{HI} = \Delta \log_{10} V_c = 0.1$, colored according to the average galaxy type in each pixel. Curved lines represent isolines of the number n of expected detections per pixel; the diagonal shading ($n < 1$) highlights the blind zone of HIPASS.

VF is dominated by gas-poor early-type galaxies, but it also predicts that HIPASS is unlikely to detect these galaxies, hence the consistent source counts. To show this explicitly, let us calculate the maximal comoving distance D_{max} (in Mpc) out to which a galaxy $\{M_{HI}, V_c\}$ can be detected, in the sense that the completeness function C drops to 50% at that distance. Substituting S_p for $10^3 S_{int} V_c^{-1}$ (approximation for $i > 45°$) and S_{int} for $4.2 \times 10^{-6} M_{HI} D_{max}^{-2}$ (approximation for $z \ll 1$), $C(S_p, S_{int}) = 0.5$ (using Equation (3)) numerically solves to $D_{max}^2 \approx 7 \times 10^{-6} M_{HI} \exp(-0.4 V_c^{0.34})$ for HICAT and NHICAT. The cosmic volume V_{max} (in Mpc^3) in which HIPASS can detect a galaxy specified by $\{M_{HI}, V_c\}$ then becomes $V_{max} \approx 0.63 \cdot (4\pi/3) D_{max}^3$, where 0.63 is the sky-coverage of HIPASS, i.e.,

$$V_{max}(M_{HI}, V_c) \approx 5 \times 10^{-8} M_{HI}^{3/2} \exp(-0.6 V_c^{0.34}). \quad (4)$$

On the other hand, the S^3-SAX model allows us to predict the space-density $\rho(M_{HI}, V_c)$ of a source $\{M_{HI}, V_c\}$, defined as the average number of sources per Mpc^3 within a pixel $\{\log_{10} M_{HI} \pm \Delta/2, \log_{10} V_c \pm \Delta/2\}$ (here using $\Delta = 0.1$). The product

$$n(M_{HI}, V_c) \equiv V_{max}(M_{HI}, V_c) \rho(M_{HI}, V_c) \quad (5)$$

then approximates the predicted number of HIPASS detections per pixel in the $\{M_{HI}, V_c\}$-plane. Figure 8 displays $\rho(M_{HI}, V_c)$ colored by galaxy type with isolines of $n(M_{HI}, V_c)$. The region $n(M_{HI}, V_c) < 1$ contains less than one detection per pixel and thus represents a "blind zone" of HIPASS. This blind zone contains the gas-poor ($M_{HI} \lesssim 10^9 M_\odot$), fast-rotating ($V_c \gtrsim 200 \, km \, s^{-1}$) early-type galaxies predicted by the model. Since HIPASS is very insensitive to these galaxies, it is simply unable to recover the predicted high-end of the VF. Surveys deeper than HIPASS are needed to verify whether the predicted amount of massive gas-poor early-type galaxies is correct. For now, it seems safe to conclude that the HIPASS VF approximates the VF of late-types, even if no Hubble-type cut is applied to the data set. On a side-note, the deeper ALFALFA survey does indeed find significant differences in the high-velocity end of the VF (e.g., Figure 4 in Papastergis et al. 2011).

In principle, the artifacts "2" and "3" of Figures 5(b) and (c) are still present in Figures 5(e) and (f), but they are occluded

by the even stronger artifacts "1" and "4." This shows that the comparison between models and observations is less prone to spurious artifacts when performed using source counts. Furthermore, within the source counts, W_{50} is a less problematic quantity than V_c due to artifact "3."

4. DISCUSSION

This section discusses the physical implications of the excellent consistency between observed and simulated H I linewidths, as well as potential applications.

4.1. Interpretation of the Consistency of W_{50}

What does the consistency between the observed and modeled W_{50}-counts (Figure 5(b)) tell us? Does it strengthen the case of the ΛCDM model or does it merely manifest the empirical tuning of the free parameters in the galaxy model? There is, as argued here, a bit of both. The local galaxy stellar MF in the model has been adjusted indirectly by tuning the feedback from star formation and black holes on the interstellar medium to reproduce the observed b_J-band and K-band LFs (Croton et al. 2006). Moreover, the radii of galaxies match the locally observed mean stellar mass-to-scale radius relation (Obreschkow et al. 2009a). One might therefore expect the galaxy rotations, which depend roughly on mass and radius, to align with local observations. In this argument, it should nonetheless be emphasized that the free model parameters (feedback coefficients and the spin ratio of baryonic matter to DM) have only been varied within the restricted ranges consistent with current high-resolution observations and high-resolution simulations. Therefore, we can at least conclude that the consistency of the W_{50}-counts in Figure 5(b) confirms ΛCDM within the current uncertainties of galaxy modeling.

Moreover, it is worth emphasizing that the relation between stellar mass and scale radius is subject to very large scatter, both observationally and in the model (Figure 2 in Obreschkow et al. 2009a). Therefore, even if the mean relation between stellar mass and scale radius is fixed to observations, this merely corresponds to an overall normalization of the VF and the corresponding W_{50}-counts. The details of these functions depend on the shape of the multi-dimensional probability-distribution of halo mass, stellar mass, and disk scale radius. This shape has not been constrained by empirical fits. Instead, it depends directly on the masses, spins, and merging histories of the dark halos in the Millennium simulation. This argument increases the support of ΛCDM.

4.2. Constraints on the Dark Matter Type

Quantifying the degree to which the W_{50}-counts support ΛCDM is of course a more delicate affair. For example, what is the actual range of allowed DM particle masses m_{DM}, assumed infinite in CDM but finite in warm dark matter (WDM) models? Answering this question would require a large array of different WDM models, similar to the Millennium simulation, equipped with SAMs, where all the uncertainties associated with every free parameter are tackled down to the W_{50}-counts. The mammoth numerical requirements of this task lie at the edge of current super-computing capacities.

Here, we limit the analysis to a first order approximation of the variation of the W_{50}-counts as a function of m_{DM}, keeping the free parameters of the galaxy-model fixed to their best values in ΛCDM. This approximation is obtained by rescaling the number density of each galaxy in S³-SAX, one-by-one, by
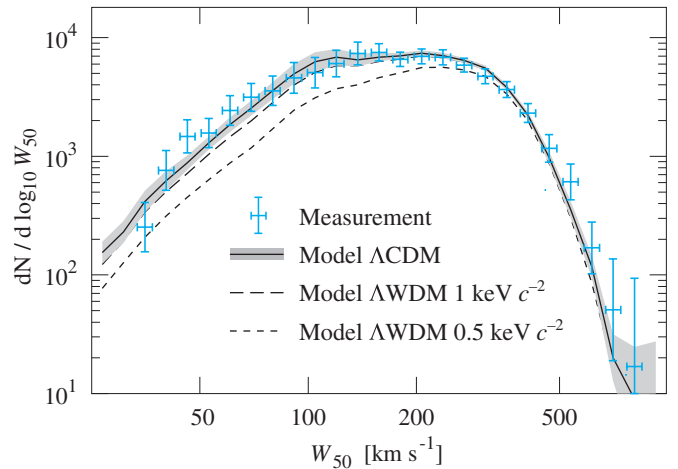
Figure 9. Analogous plot to Figure 1, but with additional lines for two alternative dark matter models assuming finite particles masses of 1 keV c^{-2} and 0.5 keV c^{-2}. The error bars sum up all the statistical and systematic uncertainties considered in this work (see Figure 5) and the gray shading denotes the standard deviation of five independent simulated reference samples for CDM.

(A color version of this figure is available in the online journal.)

$\phi_{WDM}(M_{halo})/\phi_{CDM}(M_{halo})$, where M_{halo} is the mass of the halo containing the galaxy and $\phi_{WDM}(M_{halo})$ and $\phi_{CDM}(M_{halo})$ are the local halo MFs of WDM and CDM halos, respectively. These MFs are modeled analytically by evolving the initial density field using the formulation of Sheth & Tormen (1999). WDM models are obtained by subjecting the initial CDM power spectrum to a transfer function following Bode et al. (2001). For consistency, these calculations were performed using the cosmological parameters of the Millennium simulation.

Figure 9 shows the W_{50}-counts for CDM and two WDM scenarios with particle masses $m_{DM} = 1$ keV c^{-2} and $m_{DM} = 0.5$ keV c^{-2}, respectively. Although the observed W_{50}-counts are only marginally consistent with $m_{DM} = 1$ keV c^{-2} and inconsistent with $m_{DM} = 0.5$ keV c^{-2}, those WDM cosmologies need *not* to be incompatible with the observed W_{50}-counts. In fact, we cannot exclude that varying the free parameters of the SAM within the currently allowed ranges can bring the WDM models in line with the observed data. However, Figure 9 conveys that if all free parameters in the galaxy-model can be replaced by independently determined precise values, then the W_{50}-counts from HIPASS can indeed discriminate between CDM and WDM with 1 keV c^{-2} particles.

4.3. Tully–Fisher Relation

So far, we have shown that the H I masses and circular velocities of the galaxies in the SAM (as modeled via S³-SAX) are consistent with observations, and Croton et al. (2006) showed that the stellar masses are consistent with local observations as well. However, the fact that circular velocities and masses are independently consistent with observations does not, in fact, imply that their two-dimensional distribution is correct, too. Therefore, we shall finally discuss the two-dimensional distribution of circular velocities and baryon masses, i.e., the baryonic TFR. To remain consistent with observational standards, the circular velocity is here approximated as V_{20}, defined as half the apparent H I linewidth W_{20} (measured at the 20% peak flux level), corrected for inclinations. The observational data is drawn from McGaugh et al. (2000) and corrected for $h = 0.73$. These data include galaxy types from dwarfs to giant spirals, whose values of V_{20} have been recovered from H I line measurements,
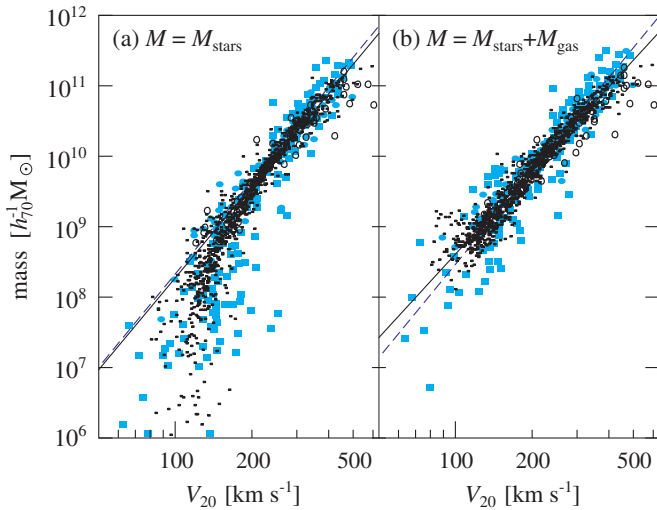
Figure 10. Relationships between edge-on H I linewidths V_{20} and two mass tracers for local galaxies. A representative sample of 10^3 simulated galaxies is shown as black points (spiral galaxies) and open circles (elliptical galaxies). Solid lines are uniformly weighted power-law fits to the simulated spiral galaxies; in Figure 10(a) this fit uses only galaxies with $M_{stars} > 10^9 h_{70}^{-1} M_\odot$. The blue dots and dashed lines are observational data and power-law fits from McGaugh et al. (2000) and references therein.

(A color version of this figure is available in the online journal.)

corrected for inclinations drawn from optical imaging. Only inclinations above $45°$ were retained to restrict the uncertainties of $\sin i$. The comparison of these data against S^3-SAX in Figure 10 reveals a good consistency, although the observational scatter is 50% larger than that of S^3-SAX. This difference is explainable by measurement uncertainties, especially regarding the inclination corrections in the low-mass end of Figure 10(a), according to McGaugh et al. (2000). Additionally, the S^3-SAX-model probably underestimates the scatter in V_{20} by ignoring the detailed substructure of H I, such as turbulent mixing in mergers, high-velocity clouds, warps, and gas-rich satellites.

Unlike the baryonic TFR (Figure 10(b)), the stellar mass TFR (Figure 10(a)) clearly departs from a power-law relation for galaxies with $V_{20} < 200 \, \text{km s}^{-1}$. As emphasized before (e.g., McGaugh et al.), this reflects the trend for high gas-fractions in low-mass galaxies and confirms that the TFR is fundamentally a relation between circular velocity and total mass, which is a function of the baryon mass (Papastergis et al. 2012).

5. CONCLUSION

This paper presented a detailed comparison between the H I lines is HIPASS and those in S^3-SAX, a cosmological model of galaxies with resolved H I lines. The results can be condensed into a list of key messages.

1. The H I linewidths of the S^3-SAX model are consistent with those measured from HIPASS (Figure 5(b)). Hence, *observed H I linewidths are consistent with ΛCDM at the resolution of the Millennium simulation* ($M_{HI} \gtrsim 10^8 M_\odot$, $V_c \gtrsim 50 \, \text{km s}^{-1}$) *within current galaxy formation models*. This does not contradict a possible breakdown of ΛCDM at smaller masses (e.g., Zavala et al. 2009).

2. Galaxies with $V_c < 50 \, \text{km s}^{-1}$ tend to be optically faint or irregular, thus suffering from large inclination uncertainties. To use these objects for physical applications, it is better compare simulations against apparent widths W_{50} rather than the inclination-corrected V_c values.

3. The model predicts that gas-poor early-type galaxies dominate the high-end of the VF. Yet the model also predicts that HIPASS is very insensitive to these galaxies because of their small M_{HI}, large W_{50} (hence higher noise), and low space-density. To test whether gas-poor early-type galaxies really dominate the high-end of the VF, deeper surveys are needed, but is seems safe to conclude that the HIPASS VF obtained using all observed galaxy types remains a VF of late-type galaxies.

4. Most sources with $W_{50} > 500 \, \text{km s}^{-1}$ in HIPASS are found to be confused; hence, confusion must be corrected in the high-end of the VF. This finding also applies to ALFALFA, because the ~ 4 times higher spatial resolution of the Arecibo beam is nearly compensated by the mean redshift being ~ 3 times higher.

5. In general, W_{50} *counts are the most reliable statistics of galaxy rotations*, since they can explicitly account for source confusion and complex completeness functions and since they are not affected by inclinations. On the downside, W_{50} counts are less sensitive to cosmological parameters than VFs, since each value of W_{50} mixes galaxies of different masses seen at different inclinations. However, the W_{50} counts of HIPASS are nonetheless sensitive to the temperature of DM.

6. In fact, if all free parameters in SAMs can be eliminated or at least constrained independently, then the W_{50}-counts derived from HIPASS can verify CDM against WDM with $1 \, \text{keV} \, c^{-2}$ particles.

These cosmological tests and prospects promise to become particularly fruitful when applied to future H I surveys, such as the full ALFALFA survey and, ultimately, the ASKAP H I All-Sky Survey (WALLABY) with the Australian Square Kilometer Array Pathfinder (ASKAP). Those future surveys should be paralleled by equally sophisticated simulated counterparts, namely mock skies produced from galaxy models extending to considerably smaller masses and circular velocities than those based on the Millennium simulation.

REFERENCES

Barnes, D. G., Staveley-Smith, L., de Blok, W. J. G., et al. 2001, MNRAS, 322, 486
Baugh, C. M., Lacey, C. G., Frenk, C. S., et al. 2005, MNRAS, 356, 1191
Blaizot, J., Wadadekar, Y., Guiderdoni, B., et al. 2005, MNRAS, 360, 159
Blake, C., Davis, T., Poole, G. B., et al. 2011, MNRAS, 415, 2892
Bode, P., Ostriker, J. P., & Turok, N. 2001, ApJ, 556, 93
Bullock, J. S., Dekel, A., Kolatt, T. S., et al. 2001a, ApJ, 555, 240
Bullock, J. S., Kolatt, T. S., Sigad, Y., et al. 2001b, MNRAS, 321, 559
Croton, D. J., Springel, V., White, S. D. M., et al. 2006, MNRAS, 365, 11
de Blok, W. J. G., Walter, F., Brinks, E., et al. 2008, AJ, 136, 2648
De Lucia, G., & Blaizot, J. 2007, MNRAS, 375, 2
Desai, V., Dalcanton, J. J., Mayer, L., et al. 2004, MNRAS, 351, 265
Doyle, M. T., Drinkwater, M. J., Rohde, D. J., et al. 2005, MNRAS, 361, 34
Driver, S. P., Hill, D. T., Kelvin, L. S., et al. 2011, MNRAS, 413, 971
Freedman, W. L., Madore, B. F., Scowcroft, V., et al. 2012, ApJ, 758, 24
Giovanelli, R., Haynes, M. P., Kent, B. R., et al. 2005a, AJ, 130, 2613
Giovanelli, R., Haynes, M. P., Kent, B. R., et al. 2005b, AJ, 130, 2598
Gonzalez, A. H., Williams, K. A., Bullock, J. S., Kolatt, T. S., & Primack, J. R. 2000, ApJ, 528, 145
Guo, Q., White, S., Angulo, R. E., et al. 2013, MNRAS, 428, 1351
Hambly, N. C., Irwin, M. J., & MacGillivray, H. T. 2001, MNRAS, 326, 1295
Jarosik, N., Bennett, C. L., Dunkley, J., et al. 2011, ApJS, 192, 14
Komatsu, E., Smith, K. M., Dunkley, J., et al. 2011, ApJS, 192, 18

Leroy, A. K., Walter, F., Brinks, E., et al. 2008, AJ, 136, 2782

Li, C., & White, S. D. M. 2009, MNRAS, 398, 2177

Loveday, J., Norberg, P., Baldry, I. K., et al. 2012, MNRAS, 420, 1239

Martin, A. M., Papastergis, E., Giovanelli, R., et al. 2010, ApJ, 723, 1359

McGaugh, S. S. 2012, AJ, 143, 40

McGaugh, S. S., Schombert, J. M., Bothun, G. D., & de Blok, W. J. G. 2000, ApJL, 533, L99

Meyer, M. J., Zwaan, M. A., Webster, R. L., Schneider, S., & Staveley-Smith, L. 2008, MNRAS, 391, 1712

Meyer, M. J., Zwaan, M. A., Webster, R. L., et al. 2004, MNRAS, 350, 1195

Obreschkow, D., Croton, D., DeLucia, G., Khochfar, S., & Rawlings, S. 2009a, ApJ, 698, 1467

Obreschkow, D., Klöckner, H., Heywood, I., Levrier, F., & Rawlings, S. 2009b, ApJ, 703, 1890

Obreschkow, D., Power, C., Bruderer, M., & Bonvin, C. 2013, ApJ, 762, 115

Obreschkow, D., & Rawlings, S. 2009, MNRAS, 394, 1857

Papastergis, E., Cattaneo, A., Huang, S., Giovanelli, R., & Haynes, M. P. 2012, ApJ, 759, 138

Papastergis, E., Martin, A. M., Giovanelli, R., & Haynes, M. P. 2011, ApJ, 739, 38

Sawala, T., Frenk, C. S., Crain, R. A., et al. 2012, arXiv e-prints

Sheth, R. K., & Tormen, G. 1999, MNRAS, 308, 119

Springel, V., White, S. D. M., Jenkins, A., et al. 2005, Natur, 435, 629

Walter, F., Brinks, E., de Blok, W. J. G., et al. 2008, AJ, 136, 2563

Wong, O. I., Ryan-Weber, E. V., Garcia-Appadoo, D. A., et al. 2006, MNRAS, 371, 1855

Zavala, J., Jing, Y. P., Faltenbacher, A., et al. 2009, ApJ, 700, 1779

Zwaan, M. A., Meyer, M. J., & Staveley-Smith, L. 2010, MNRAS, 403, 1969

Zwaan, M. A., Meyer, M. J., Staveley-Smith, L., & Webster, R. L. 2005, MNRAS, 359, L30

Zwaan, M. A., Meyer, M. J., Webster, R. L., et al. 2004, MNRAS, 350, 1210

Zwaan, M. A., Staveley-Smith, L., Koribalski, B. S., et al. 2003, AJ, 125, 2842